# OPTICAL FLASHES AND RADIO FLARES IN GAMMA-RAY BURST AFTERGLOW: NUMERICAL STUDY

SHIHO KOBAYASHI

Department of Earth and Space Science, Osaka University, Toyonaka, Osaka 560, Japan; shiho@vega.ess.sci.osaka-u.ac.jp

AND

RE'EM SARI

Theoretical Astrophysics 130-33, California Institute of Technology, Pasadena, CA 91125; sari@tapir.caltech.edu

## ABSTRACT

The strong optical flash observed by ROTSE, as well as the radio flare associated with GRB 990123 can be attributed to the emission of the fireball ejecta, initially heated by the reverse shock. We numerically study the evolution of an adiabatic relativistic fireball interacting with an ambient uniform medium, both in the initial energy transfer stage and in its late evolution. It is shown that the Blandford-McKee solution adequately describes the evolution of the shocked shell quite early on and for as long as the fireball material has relativistic temperatures. In the case where the reverse shock is only mildly relativistic, the shocked shell becomes cold almost immediately and the evolution deviates from the Blandford-McKee solution. We derive analytical expressions for the ejecta evolution in its cold regime. This solution gives a good approximation to the numerical results. We estimate the radiation from the fireball ejecta using the numerical hydrodynamic evolution in both cases: cold and hot shells. Surprisingly, we find that both evolutions give rather similar light curves, decaying approximately as $T^{-2}$ in the optical and peaking at about 1 day in the radio, even though the hydrodynamics is different.

*Subject headings:* gamma rays: bursts — hydrodynamics — relativity — shock waves

*On-line material:* color figures

## 1. INTRODUCTION

Precise and prompt gamma-ray burst localization by an Italian-Dutch satellite, *BeppoSAX*, makes it possible for other space and ground instruments to scan the same direction. The long-lasting counterparts (afterglows) in X-ray, optical, and radio wavelengths have been detected. Up to the event of GRB 990123, the overall behavior of the afterglows could be explained reasonably well by the synchrotron emission from the ambient medium particles (ISM) that are shocked by the relativistic flow.

GRB 990123 is the brightest gamma-ray burst seen by *BeppoSAX*, and the fluence is in the top 0.3% of all bursts observed so far (Kippen et al. 1999). Absorption lines in the optical afterglow gave a lower limit of the redshift $z > 1.6$, the energy required to produce the bright gamma-ray burst is enormous, $3 \times 10^{54}$ ergs for an isotropic emission. A new clue to understand the nature of gamma-ray bursts was found in this event by ROTSE which detected a strong optical flash during the "gamma-ray" burst. ROTSE started to observe the direction in an optical band 22 s after the onset of the burst. The optical flash reached to a peak of ninth magnitude and then decayed with a slope of a power-law index ~2 (Akerlof et al. 1999).

Such a strong prompt optical flash was predicted (Mészáros & Rees 1997; Sari & Piran 1999a, 1999b). The prompt optical flash observed by ROTSE is compatible with these predictions (Sari & Piran 1999c; Mésáros & Rees 1999). In the energy transfer stage of a fireball evolution, the forward-shocked ISM and the reverse-shocked fireball shell carry a comparable amount of internal energy. However, the typical temperature in the shocked ejecta is considerably lower than that of the shocked ISM. Consequently, the typical frequency of the synchrotron emission from the shocked shell is much lower than that from the shocked ISM, and it comes to the optical band with reasonable values of the parameters.

Beside the optical flash, GRB 990123 had another newly observed phenomenon, a radio flare (Kulkarni et al. 1999). While the usual radio afterglows rise on timescale of weeks or months, this burst had a radio flare peaking at 1 day, rising quickly before the peak and decaying quickly after the peak. Sari & Piran (1999c) have interpreted this flare as the emission from the ejecta particles earlier shocked by the reverse shock. The same particles producing the prompt optical flash have been cooled adiabatically, and their emission shifts quickly toward lower frequencies while weakening. According to the analytical estimates of Sari & Piran, scaling the prompt optical emission to the epoch of the radio detection gives the right amount of radio emission.

The discussion of the prompt optical flash is quite robust, but the estimate of the hydrodynamical evolution of the shocked ejecta is more fragile. In this paper we study numerically the energy transfer stage and the evolution of the ejecta after that in order to estimate the decay rate of the optical flash as well as the light curve and timing of the radio flare. We consider both cases where the temperature of the shocked shell is relativistic or not. Using equipartition assumption on the magnetic field we construct the light curve of the emission from the shell. In § 2, we shortly review the hydrodynamics of a fireball. We show in § 3 the analytic estimate of the evolution of the shocked ejecta for both case of the hot and the cold shell case. The radiation from the ejecta is also estimated. In § 4, we discuss the numerical results. Finally, in § 5 we summarize the results and discuss their implications.

## 2. HYDRODYNAMICS OF A FIREBALL

The evolution of an adiabatic spherical fireball with an

energy $E$ and a dimensionless entropy (or random Lorentz factor) $\eta$ and a radius $R_0$ is characterized by several phases (Kobayashi, Piran, & Sari 1999). Initially, as the fireball expands into a surrounding medium with a low-density $\rho_1$, a narrow shell with a radial width of $\Delta \sim R_0$ is formed. The Lorentz factor of the shell increases linearly with the radius during the free acceleration stage. At $R_L \equiv R_0 \eta$ the fireball shell uses up all its initial radiation energy, it coasts with the Lorentz factor of $\eta$ and the frozen radial width $\Delta \sim R_0$. The coasting ends once the ISM begins to influence the shell. The interaction between the shell and the ISM is described by two shocks: a forward shock propagating into the ISM and a reverse shock propagating into the shell.

A dimensionless quantity $\xi \equiv (l/\Delta)^{1/2}/\eta^{4/3}$ is useful to consider the evolution of the fireball shell after the coasting stage (Sari & Piran 1995) where $l \equiv (E/\rho_1 c^2)^{1/3}$ is the Sedov length. The evolution can be classified into two categories by this quantity. We call the case of $\xi > 1$ the Newtonian reverse shock (NRS) case, and $\xi < 1$ the relativistic reverse shock (RRS) case.

If initially $\xi > 1$ (the NRS case), the coasting shell begins to spread as $\Delta \sim R/\eta^2$ at $R_s \equiv R_0 \eta^2$ due to a slight difference of the velocity inside the shell. The reverse shock is initially Newtonian and becomes mildly relativistic when the reverse shock crosses the shell. After the crossing which happens at $R_\gamma \equiv l/\eta^{2/3}$, the forward-shocked ISM has the most energy of the system.

If initially $\xi < 1$ (the RRS case), the reverse shock becomes relativistic at $R_N = l^{3/2}/\Delta^{1/2}\eta^2$, which is before the shock crosses the shell. At $R > R_N$ the reverse shock begins to reduce considerably the Lorentz factor of the shell's matter which it crosses. The distance between the contact discontinuity and the reverse shock is $\propto R^2$, where $R$ is the forward shock radius. After the drastic deceleration, during the shock crossing, the shocked shell slows down as $\propto R^{-1/2}$ due to the pressure difference between the forward shock and the reverse shock. At $R_\Delta \equiv l^{3/4}\Delta^{1/4}$, the shock crosses the whole shell and most of the energy of the system has been transferred to the forward-shocked ISM. The spreading effect is not important in this case since the spreading radius $R_s$ is larger than $R_\Delta$.

Kobayashi et al. (1999) have shown numerically that after $R_\gamma$ for the NRS case or $R_\Delta$ for the RRS case, the profile of the shocked ISM begins to approach the Blandford-McKee solution (Blandford & McKee 1976, hereafter BM) which is the basis of most of the afterglow theories. The fraction of the energy of the ejecta rapidly decays as the forward-shocked ISM has most of the energy in the system. We are interested in the evolution of this reverse-shocked ejecta as the source of the rapidly decaying optical flash and the radio flare (Sari & Piran 1999c; Kulkarni et al. 1999).

## 3. LATE EJECTA EVOLUTION—ANALYTICAL ESTIMATES

### 3.1. Hydrodynamics—Relativistic Temperatures

In the previous section we discussed the hydrodynamical evolution of the ejecta up to the time that a considerable fraction of the energy was given to the surrounding medium. Beyond this time, one has to calculate the evolution of the Lorentz factor, the pressure (or the energy density) and the mass density as functions of time in order to evaluate the emission from the ejecta. Sari & Piran (1999b, 1999c) used the Blandford-McKee solution to estimate all these quantities. Using this solution, the Lorentz

factor, the pressure, and the mass density of a fluid element are given by

$$\gamma \propto R^{-7/2}, \quad p \propto R^{-26/3}, \quad \rho \propto R^{-13/2}. \quad (1)$$

Since the observer time is given by $T \propto R/\gamma^2 c \propto R^8$, we obtain $\gamma \propto T^{-7/16}, p \propto T^{-13/12}$ and $\rho \propto T^{-13/16}$.

Sari & Piran (1999c) found good agreement between the light curves derived with the above scalings and the observed optical flash and radio flare. However, it is not clear whether the BM solution is applicable to the reverse-shocked ejecta for the following reasons. (i) The BM solution, as a self-similar solution, describes the shocked ISM long after the energy transfer stage where the details of the initial conditions are no longer important. (ii) It assumes that the initial shell is irrelevant, however, the evolution of that shell is what we are interested in. (iii) The initial shell contains much more particles than those collected by the forward shock. Its density therefore must be higher than that predicted by the BM solution. (iv) Though the BM solution assumes relativistic temperatures, a mildly relativistic reverse shock cannot heat ejecta to such a high temperature.

It can be argued that since the shocked ejecta is located not too far behind the forward shock at the end of the energy transfer stage and it has a comparable amount of energy to that of the system, it roughly fits the BM solution. The fact that its rest mass density is much higher than that given by the BM solution should not play an important role as long as the temperature is relativistic. At relativistic temperature, the fluid inertia is due to its thermal energy rather than the rest mass. The fluid therefore can be expected to evolve according to the BM scalings with density that is higher by a constant factor from that given by the BM solution. We will show numerically that indeed the points (i)–(iii) raised above are not a real problem, and the BM solution adequately describes the evolution of the ejecta from the very early stage as long as its temperature is relativistic. The fourth point, however, i.e., the underlying assumption of the BM solution that the temperature is relativistic, might become incorrect quite early on. Specifically, if the reverse shock is only mildly relativistic, this assumption breaks from the beginning and the BM solution cannot describe any of the ejecta evolution.

Mészáros & Rees (1999) assumed a general power-law evolution of the forward shock and approximated the ejecta Lorentz factor to be equal to that of the forward shock, $\gamma \propto R^{-g}$. The density was estimated by assuming that the ejecta spreads in the local frame by the speed of light, the width in the local frame is therefore $R/\gamma$. Since the number of particles there is constant, the density drops as $n \propto R^{-3}\gamma \propto R^{-3-g}$. They considered two possible evolutions of the pressure. (I) The "pressure equilibrium" assumption that the ejecta pressure is equal to the forward shock pressure, leads to $p \propto \gamma^2 \propto R^{-2g}$. (II) Adiabatic expansion $p \propto \rho^{4/3}$. In terms of observed time these scalings are $\gamma \propto T^{-g/(1+2g)}$, $\rho \propto T^{-(3+g)/(1+2g)}$ and $p \propto T^{-2g/(1+2g)}$ for the "pressure equilibrium" and $p \propto T^{-4(3+g)/3(1+2g)}$ for the "adiabatic expansion."

In the section below we show that $g$ is constrained to the range $3/2 \leq g \leq 7/2$. Note, that even though this seems as a large range, when translating this to $\gamma$ as function of the observed time $T$ rather than the radius $R$, we obtain a considerable more narrow range of $T^{-0.375}$ to $T^{-0.4375}$. The observable, as function of the observed time, are there-

fore not very sensitive to the exact value of $g$. For $g = 7/2$ one obtains the deceleration law of the Lorentz factor and the temporal evolution of the density of a fluid element in the BM solution follows. That is, the BM solution satisfies the spreading assumption. Furthermore, the BM solution satisfies the adiabatic expansion law, $p \propto \rho^{4/3}$. Note also that though the power law $\gamma \propto R^{-g}$, with $g = 7/2$ agrees with the BM evolution of a given fluid element, $g = 7/2$ does not describe the Lorentz factor of the shock, which evolves as usual with $R^{-3/2}$.

### 3.2. Hydrodynamics—Subrelativistic Temperatures

None of the two papers above considered the sub-relativistic temperature regime. As mentioned earlier this regime can be important quite early on if the reverse shock is mildly relativistic. It is impossible to repeat the analysis of Sari & Piran (1999a, 1999b) since there is no known analytical solution describing this regime. The BM solution is not applicable since the temperature is nonrelativistic and the Sedov-Taylor solution is not applicable as the bulk Lorentz factor of the fluid is relativistic. However, we can minimize the uncertainty to a single parameter in a restricted range.

Assume as above that $\gamma \propto R^{-g}$. If $\gamma$ is not described by a power law of $R$, a limited range of radius is considered over which the value of $g$ is approximately a constant. We can expect $g$ to be higher than $3/2$, since the ejecta must lag behind the forward shock, but we can expect $g < 7/2$ as compared to the BM solution, since the ejecta has higher inertia (due to its non-negligible rest mass), and therefore they are expected to be slowed down less abruptly.

We can now use a version of the spreading assumption as follows: when the ejecta arrives at radius $R$ the time in the local frame is $R/c\gamma$. The ejecta sound speed is subrelativistic and can be estimated by $(p/\rho)^{1/2}$. The width of the shell will therefore be $(p/\rho)^{1/2}R/c\gamma$. The ejecta density is therefore: $\rho \propto R^{-3}\gamma(\rho/p)^{1/2}$. Using the adiabatic expansion law $p \propto \rho^{4/3}$, we get

$$\gamma \propto R^{-g}, \quad p \propto R^{-8(3+g)/7}, \quad \rho \propto R^{-6(3+g)/7}. \quad (2)$$

In terms of the observer time these scalings become $\gamma \propto T^{-g/(1+2g)}$, $p \propto T^{-8(3+g)/7(1+2g)}$, and $\rho \propto T^{-6(3+g)/7(1+2g)}$.

We note that the above derivation is not rigorous. A power-law evolution of $\gamma$ as function of radius is not necessarily correct in the subrelativistic temperature regime. Moreover, the spreading assumption may not be valid if the pressure gradients in the ejecta are steep. We therefore use the above only as a guiding line to compare with the numerical results.

We assumed above (and through the paper) that the fluid is described by a constant adiabatic index $\hat{\gamma} = 4/3$. This is clearly true as long as the protons are relativistic. Once the shell is cold and the protons are no longer relativistic, their adiabatic index becomes $\hat{\gamma} = 5/3$. A mixture of Newtonian protons and relativistic electrons results in adiabatic index of $\hat{\gamma} = 13/9$ if the two species are kept in equipartition. However, the basic assumption here is that some level of equipartition is only created by the passage of a shock since the collision time is too long. Once the protons become Newtonian and their adiabatic index becomes $\hat{\gamma} = 5/3$, electrons and protons will deviate from equipartition since they evolve differently. They always have the same density due to the charge neutrality but the thermal energy of protons evolves as $\rho^{5/3}$, while that of the electrons evolves as $\rho^{4/3}$. As $\rho$ decreases, the relativistic electrons dominate the thermal energy and the pressure of the fluid. Since the electrons are

still relativistic far after the protons become cold we assume that the fluid is described by a constant adiabatic index $\hat{\gamma} = 4/3$, even after the shell become cold with Newtonian protons.

### 3.3. The Ejecta Emission

The reverse shock propagates into the shell and heats its electrons. After it has crossed the shell, no new electrons are injected. The emission from the reverse-shocked shell reaches the peak at $R_{\gamma}$ for a NRS case ($\xi > 1$) or $R_{\Delta}$ for a RRS case ($\xi < 1$). Since the Lorentz factor of the shocked region at that time is $\eta$ and $\xi^{3/4}\eta$, respectively, the peak time for the observer is given by $\xi^{2}R_{0}/c$ and $R_{0}/c$, respectively. According to the internal shock model the duration of the gamma-ray burst itself is $R_{0}/c$.

After the peak time when the reverse shock crossed the shell, the shocked electrons cool radiatively and adiabatically. We consider here the simplest case in which the energy of the magnetic field remains a constant fraction of the internal energy $B^{2} \propto p$. The electron random Lorentz factor evolves as $\gamma_{m} \propto p/\rho$ due to the adiabatic expansion. The typical synchrotron frequency in the observer frame is $\nu_{m} \propto \gamma\gamma_{m}^{2}B$, the spectral power at the typical frequency is $F_{\nu_{m}} \propto \gamma B$ for a fixed total number of radiating electrons. Assuming a power-law distribution of the electron random Lorentz factor with index $\hat{p}$, the spectral flux at a given frequency above $\nu_{m}$ is $F_{\nu} \sim F_{\nu_{m}}(\nu/\nu_{m})^{-(\hat{p}-1)/2}$, while below $\nu_{m}$ we have the synchrotron low-energy tail as $F_{\nu} \sim F_{\nu_{m}}(\nu/\nu_{m})^{1/3}$. Substituting the expressions for $\nu_{m}$ and $F_{\nu_{m}}$ we have

$$F_{\nu} \propto \begin{cases} \gamma^{2/3}p^{-1/3}\rho^{2/3} & \nu < \nu_{m}; \\ \gamma^{(\hat{p}+1)/2}p^{(5\hat{p}-3)/4}\rho^{-(\hat{p}-1)} & \nu > \nu_{m}. \end{cases} \quad (3)$$

This is a generalized form of equation (3) in Sari & Piran (1999c) in which they substituted the BM relations and $\hat{p} = 2.5$ to get a $T^{-2.1}$ decay above $\nu_{m}$ and a $T^{-17/36}$ below $\nu_{m}$.

If the power-law scalings (eq. [2]) are valid, typical frequency $\nu_{m}$ and the peak flux $F_{\nu_{m}}$ evolve as $\nu_{m} \propto T^{-3(8+5g)/7(1+2g)}$ and $F_{\nu_{m}} \propto T^{-(12+11g)/7(1+2g)}$. The flux at a frequency below $\nu_{m}$ (above $\nu_{m}$) drops as $T^{-2(2+3g)/7(1+2g)}$ ($T^{-(7+24\hat{p}+15\hat{p}g)/14(1+2g)}$). These decay indexes of the flux are monotonic functions of $g$ and are not so sensitive to it. If the value of $g$ is limited as $3/2 < g < 7/2$, these vary in relatively narrow ranges for $\hat{p} = 2.5$. The index for the low-frequency part is between $-0.46$ and $-0.44$, the index for the high part is between $-2.2$ and $-1.8$. These are very close to the estimates from the BM scalings.

At low frequencies and early times, self-absorption takes an important role and significantly reduces the flux. A simple estimate of the maximal flux is the emission from the black body with the reverse shock temperature. The temperature is given by the random energy of the typical electron $m_{e}c^{2}\gamma_{m}$ for a frequency below the typical frequency $\nu_{m}$. If the observed radio frequency is above it, the electron radiating into the observed frequency has energy higher by a factor $(\nu/\nu_{m})^{1/2}$ since the synchrotron emission frequency is proportional to the square of the Lorentz factor. Using the same expression as in Sari & Piran (1999c), but leaving arbitrary the hydrodynamic evolution, we get an upper limit to the emission of

$$F_{\nu} \cong 5.0 \times 10^{-8}(\text{Jy})\gamma^{3}\gamma_{e} \max\left[1, \left(\frac{\nu}{\nu_{m}}\right)^{1/2}\right]$$

$$\times \left(\frac{T}{1 \text{ day}}\right)^{2}\left(\frac{\nu}{8.5 \text{ GHz}}\right)^{2}, \quad (4)$$

where we assumed $\Omega_0 = 1$, $\lambda_0 = 0$, $h = 0.65$ and the location of the fireball $z = 1.6$ as GRB 990123. The emission will therefore be the minimum between that given by equations (3) and (4).

Since our numerical simulation is purely hydrodynamic, we cannot use them to verify any of the radiation assumptions leading to equations (3) and (4). We will therefore use the above expression to evaluate the output radiation from the hydrodynamical properties of the ejecta. However, we will be able to get a more realistic hydrodynamic by using the numerical simulations.

## 4. NUMERICAL SIMULATION

The initial configuration for our simulation is a static uniform spherical fireball surrounded by a uniform cold ISM. It is determined by four parameters: a total energy $E$, a dimensionless entropy $\eta$, an initial radius $R_0$, and an ISM density $\rho_1$. $E$ and $\rho_1$ always appear as the ratio of $E/\rho_1$ in the hydrodynamics computation, the system is actually determined by three parameters, the initial radius $R_0$, the entropy $\eta$ and the Sedov length $l$. First we consider two extreme cases—RRS $\xi \ll 1$ and NRS $\xi \gg 1$—to see the difference clearly. Then, the case of GRB 990123 will be studied.

### 4.1. The Relativistic Reverse Shock Case

The temperature of the reverse-shocked ejecta is one of the differences between the RRS case and the NRS case. We suspect that the relativistic temperature is a crucial condition to apply the BM solution to the shocked ejecta. We consider a relativistic reverse shock case $E = 3 \times 10^{54}$ ergs, $\rho_1 = 10$ protons cm$^{-3}$, $\eta = 2 \times 10^5$ and $R_0 = 3 \times 10^{10}$ cm, and we compare the evolution of the ejecta with the BM solution. This parameter set corresponds to $\xi = 10^{-3}$.

For computational efficiency, this simulation is started at $R_\Delta/100 \sim 5 \times 10^{14}$ cm at which the ejecta shell is in the coasting stage. It is larger than $R_N \sim 2 \times 10^{12}$ cm where the reverse shock becomes relativistic, but at that time only $10^{-6}$ of the ISM material within $R_\Delta$ had been swept up. In other word, the reverse shock had decelerated $10^{-4}$ of the shell (Sari & Piran 1995; Kobayashi et al. 1999). Therefore, the deceleration prior to this time can be neglected.

Initially, the unshocked fireball shell has all the energy of the system. As the shell expands, the reverse shock decelerates the ejecta while the forward shock accelerate the ISM. The energy is transferred from the unshocked shell to the ISM via the shocks, finally the shocked ISM carries all the energy of the system. In the intermediate stage, around $R_\Delta$, the shocked shell has comparable energy to the shocked ISM. The evolutions of the energies in three regions, inside of the reverse shock (unshocked shell), between the reverse shock and the contact discontinuity (shocked shell), and between the contact discontinuity and the forward shock (shocked ISM) are shown in Figure 1.

We numerically define the reverse shock crossing time $R_{\Delta,\text{num}}$ as the time at which the energy in the shocked shell becomes equal to the unshocked one. $R_{\Delta,\text{num}}$ is $\sim 3.3 \times 10^{16} \sim 0.7 R_\Delta$ cm in this case. The profile at $R_{\Delta,\text{num}}$ is plotted in Figure 2, we can clearly see the forward and the reverse shock and the contact discontinuity. The widths of the shocked ISM and the shocked fireball are comparable, the analytical estimate is $\sim R_0/2 = 1.5 \times 10^{10}$ cm.

The Lorentz factor of the shocked shell is about 700, which is comparable to the analytic estimate $\xi^{3/4}\eta \sim 1100$.
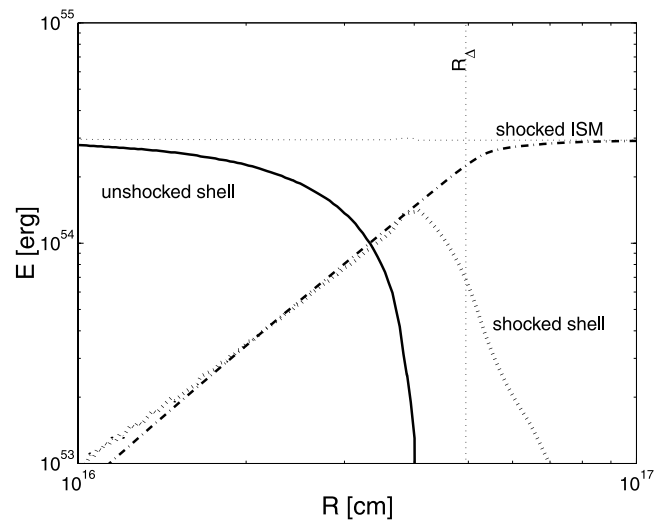


FIG. 1.—Energy transfer from the fireball to the shocked regions. The sum of the kinetic and the thermal energies in the unshocked shell (*solid line*), in the reverse-shocked shell (*dotted line*) and in the forward-shocked ISM (*dash-dotted line*). The horizontal dotted line is the sum of the energies in the three region. $R_\Delta$ (*vertical dotted line*) is a analytic estimate where the reverse shock crosses the ejecta. See the electronic edition of the Journal for a color version of this figure.
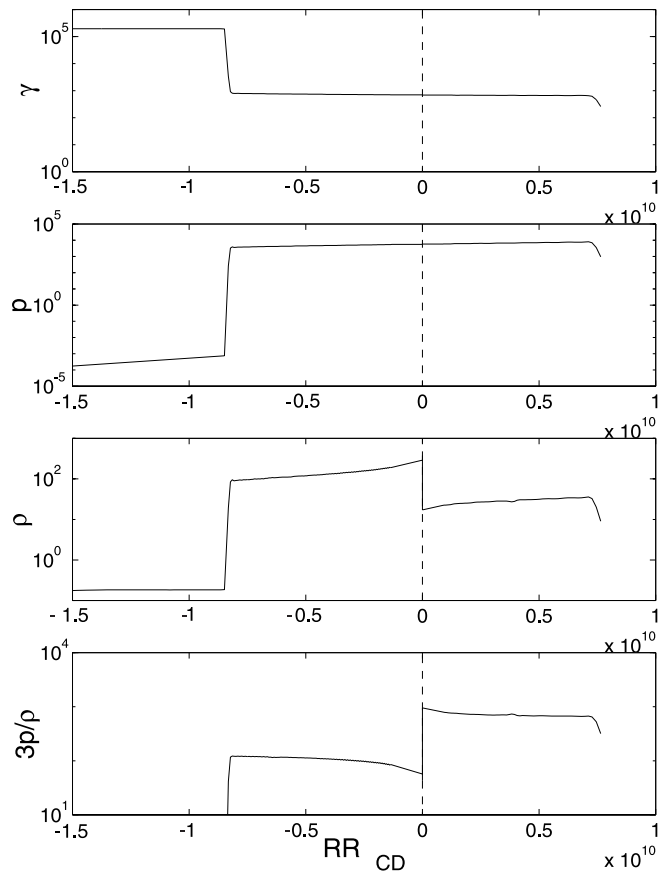


FIG. 2.—Profile: Lorentz factor, pressure, density, and random Lorentz factor at the crossing time, $R_{\Delta,\text{num}}$. The x-axis is the distance from the contact discontinuity. See the electronic edition of the Journal for a color version of this figure.

There is a jump of the density at the contact discontinuity while pressure is almost constant through the shocked regions, then the random Lorentz factors (or the temperature) $e/\rho$ are different between the shocked regions separated by the discontinuity. The numerical values are about 100 in the reverse-shocked region and 700 in the forward-shocked region, while the analytic estimates are $\xi^{-3/4} \sim 180$ and $\xi^{3/4}\eta \sim 1100$, respectively.

In the BM solution, the Lorentz factor, the density, and the pressure are given by

$$\gamma/\gamma_2 = \chi^{-1/2}, \quad p/p_2 = \chi^{-17/12}, \quad \rho/\rho_2 = \chi^{-5/4}, \quad (5)$$

where $\gamma_2$, $p_2$, and $\rho_2$ are the values of the Lorentz factor, the pressure, and the density just behind the forward shock and the similarity variable $\chi$ is defined by $\chi \equiv 1 + 16\gamma_2^2(t)$ $[1 - r/R(t)]$ with the shock radius $R(t)$. Radius $r$ and time in the observer's rest frame $t$ are independent coordinates here. After the reverse shock crossed the shell at $\sim R_{\Delta,\mathrm{num}}$, a rarefaction wave begins to propagate from the inner edge of the shell, crosses the contact discontinuity and continues toward the forward shock. Around $2R_{\Delta,\mathrm{num}}$, it reaches the forward shock, the separation between the contact discontinuity and the forward shock becomes comparable with the thickness of the blast wave $R/4\gamma_2^2$. Then, the profile of the forward-shocked region approaches the BM solution. The profiles normalized by the value just behind the forward shock at different times are plotted in Figure 3. The boundaries of the ejecta shell are indicated by the filled and the open circles. The former is the contact discontinuity, the latter marks the fluid element in which the reverse shock has been at time $R_{\Delta,\mathrm{num}}$.

The profile of the reverse-shocked ejecta except the density one (the right side of the filled circle) also approaches that of BM. This can be understand as follows, since the temperature of the shocked ejecta is relativistic, the internal energy dominates the fluid inertia. The density jump at the contact discontinuity is negligible for the evolution of the ejecta since its inertia is given by its internal energy rather than its rest mass and the BM solution fits the profile. The evolution of the Lorentz factor, the pressure, and the density of the ejecta shell are plotted in Figure 4. After the rarefaction wave reaches the forward shock around $2R_{\Delta,\mathrm{num}}$, the scalings of the ejecta are also adequately approximated by the BM scalings for a fluid element.

We define the effective scaling indexes, $-R/\gamma \cdot d\gamma/dR$, $-R/p \cdot dp/dR$, and $-R/\rho \cdot d\rho/dR$. The evolutions of the averaged values in the shocked shell are plotted against the radius of the forward shock in Figure 5. The scaling index of the Lorentz factor $g$ is about 3 rather than the $7/2$ of the BM solution, after the rarefaction wave reaches the forward shock. The dotted lines depict the analytic estimate (eq. [2]) assuming the numerical index $g$. The analytic estimate fits the numerical results as long as the bulk motion is relativistic, the spreading assumption and the adiabatic expansion law are therefore a good approximation.

The optical flash of GRB 990123 initially decayed as $T^{-2}$. This implies that the typical synchrotron frequency is already below the optical band at the peak. In order to compare with the result in GRB 990123 case later, we plot the light curve for a frequency above the typical one in Figure 6, where we used the high-frequency part ($v > v_m$) of equation (3). The steepness of the light curve is about $-2$ at late time with a steeper slope at early times when the rarefaction wave is going through the shell.
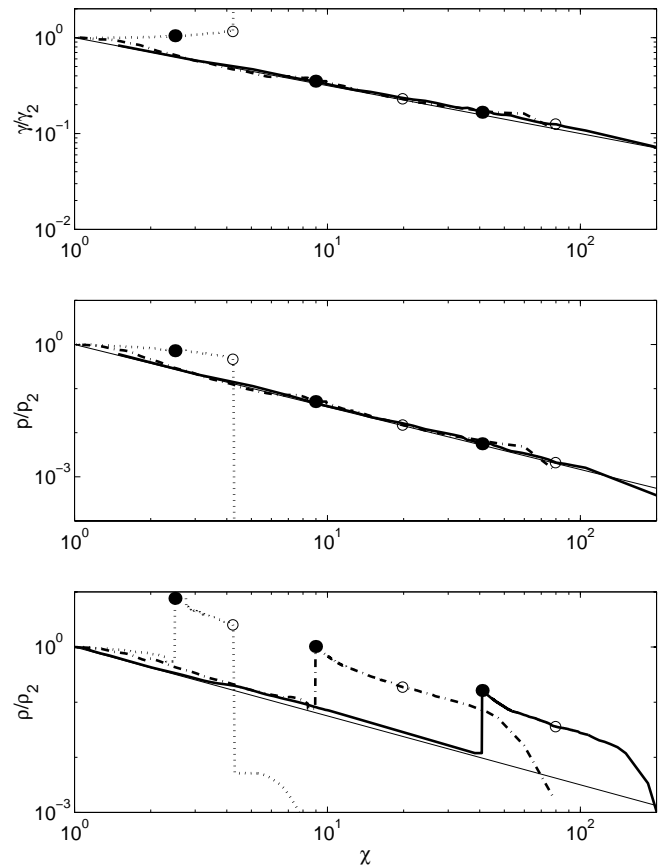


FIG. 3.—RRS case: Lorentz factor, pressure, and density as functions of $\chi$ at $R_{\Delta,\mathrm{num}}$ (dotted lines), at $2R_{\Delta,\mathrm{num}}$ (dot-dashed lines) and at $3R_{\Delta,\mathrm{num}}$ (solid lines). The Blandford-McKee solution is the thin solid lines. The ejecta shell is bounded by the contact discontinuity (filled circle) and the fluid element where the reverse shock is at $R_{\Delta,\mathrm{num}}$ (open circle). $\gamma$, $p$, and $\rho$ are normalized with $\gamma_2$, $p_2$, and $\rho_2$, which are numerical values just behind the forward shock. See the electronic edition of the Journal for a color version of this figure.

## 4.2. The Newtonian Reverse Shock Case

We consider the other extreme case in which the shocked ejecta is cold from the beginning. The initial condition is $E = 3 \times 10^{54}$ ergs, $\rho_1 = 10$ protons cm$^{-3}$, $\eta = 10^3$, and $R_0 = 3 \times 10^7$ cm. This corresponds to the NRS case of $\xi = 44$.

In the NRS case, the energy of the ejecta is transferred to the ISM when the forward shock collects ISM mass of $E/\eta^2$ around $R_\gamma \sim 6 \times 10^{16}$ cm. The reverse shock crosses the ejecta at the same time. The numerical estimate is $R_{\Delta,\mathrm{num}} \sim 3 \times 10^{16}$ cm.

The Lorentz factors of the shocked regions are about 700 at that time. The reverse-shocked ejecta is already cold $3p/\rho \sim 0.05$, while the forward-shocked ISM is hot $3p/\rho \sim 700$. The profiles at different times are plotted against the similarity variable $\chi$ in Figure 7. At $\sim 2R_{\Delta,\mathrm{num}}$ the forward-shocked region is relatively well described by the BM scaling, but there is a break at the contact discontinuity and the reverse-shocked region deviates from it. The reverse shock does not heat the shell well, the pressure of the shocked region is less than the value expected from the BM solution. The evolution of $\chi_e$ for a fixed element in the BM solution is given by $\chi_e = \chi_{e0}(R/R_0)^4$, where $R_0$ and $\chi_{e0}$ are the initial shock radius and the initial value of $\chi$. At $R_{\Delta,\mathrm{num}}$, the boundaries of the shell are at $\chi = 2.5$ and $2.7$, the analy-
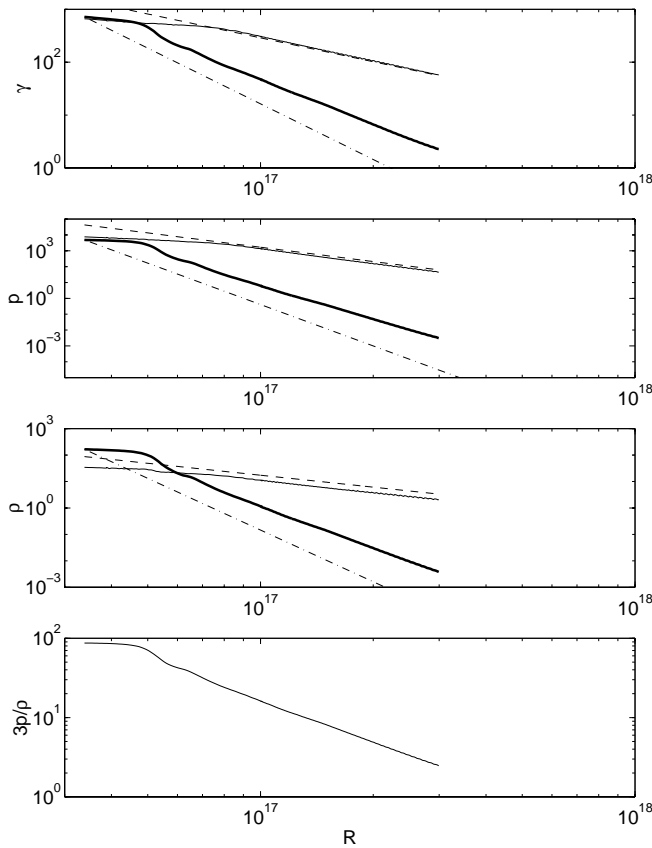
FIG. 4.—Evolution of Lorentz factor, pressure and density: RRS case. The numerical values just behind the forward shock are the thin solid lines, the expected values from the Blandford-McKee solution are the thin dashed lines. The numerical evolution of the averaged values in the ejecta shell (*thick solid lines*) are compared with the Blandford-McKee scalings of a fluid element (*thin dash-dotted lines*). See the electronic edition of the Journal for a color version of this figure.
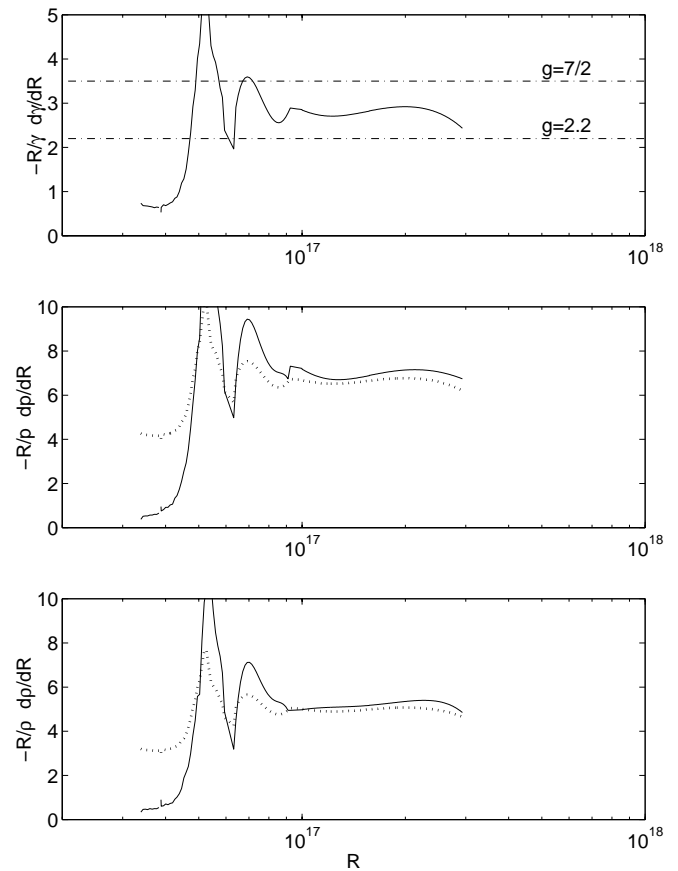
FIG. 5.—Effective scaling indexes vs. Radius of the shell: RRS case. The numerical results are the solid lines. The dotted lines in the middle and the bottom panel are analytic estimates assuming the numerical index $g$. See the electronic edition of the Journal for a color version of this figure.

tic formula gives that the values are 40 and 43 at $2R_{\Delta,\mathrm{num}}$, 203 and 219 at $3R_{\Delta,\mathrm{num}}$. However, the shocked ejecta departs from the forward shock slower, the numerical correspondences are 4.5 and 4.6 at $2R_{\Delta,\mathrm{num}}$, 8.3 and 8.4 at $3R_{\Delta,\mathrm{num}}$.

The profile of the shocked regions does not deviate from the self-similar scalings so much in Figure 7, but the evolution of $\chi_e$ is much slower. The hydrodynamic variables of the shocked shell evolve slower. In Figure 8 the averaged values of the Lorentz factor, the pressure, and the density in the shell are compared with the BM solution (eq. [1]). Though the values just behind the forward shock (*thin solid line*) fit the BM scalings well around $2R_{\Delta,\mathrm{num}}$, the numerical scaling (*thick solid line*) is very different from the BM one for a fluid element. The effective scaling index of $\gamma$ is about 2.2 as we can see in Figure 9. The analytic estimates (eq. [2]) based on the spreading assumption and the adiabatic expansion are a good approximation as long as the bulk motion is relativistic.

We plot the light curve for a frequency above the typical one in Figure 6. The light curve is approximated by $T^{-2}$ very well.

### 4.3. GRB 990123

We have seen the two extreme cases: the RRS ($\xi \ll 1$) and the NRS ($\xi \gg 1$). In the RRS case the BM solution can describe well the evolution of the shocked ejecta, but the scalings of the NRS are very different from the BM. The fireball of GRB 990123 is actually a marginal case as we shall soon see. However, such marginal cases behave very much like the NRS, since the shell becomes cold at the early stage.

According to the internal shocks model, the duration of the gamma-ray burst is determined by the thickness of the relativistic flow which is the initial fireball size. The $T_{90}$ duration of GRB 990123 is 63 s in the 50–300 keV range (Galama 1999). The burst profile is dominated by two peaks, each lasting 8 s, separated by 12 s, we assume $R_0/c = 40$ s. The observations suggest that the typical synchrotron frequency of the reverse shock is below the optical bands quite early on, then the initial Lorentz factor of the ejecta is a few hundred (Sari & Piran 1999c). $\eta = 400$ is assumed here. The explosion energy and the ambient density are rather uncertain. We assume $E = 1 \times 10^{54}$ ergs and $\rho_1 = 5$ protons cm$^{-3}$. This is a marginal case of $\xi = 0.7$.

The explosion energy might be higher, since the internal shocks cannot convert the whole kinetic energy of the flow into the thermal energy and only some part of thermal energy goes into random motions of the electrons (Kobayashi, Piran, & Sari 1997). However, the Sedov length determining the hydrodynamic timescale is relatively insensitive to $E$. A nonspherical (jet) geometry of the ejecta is suspected from the break in the afterglow light curve (Kulkarni et al. 1999). Even in this case, a spherical fireball
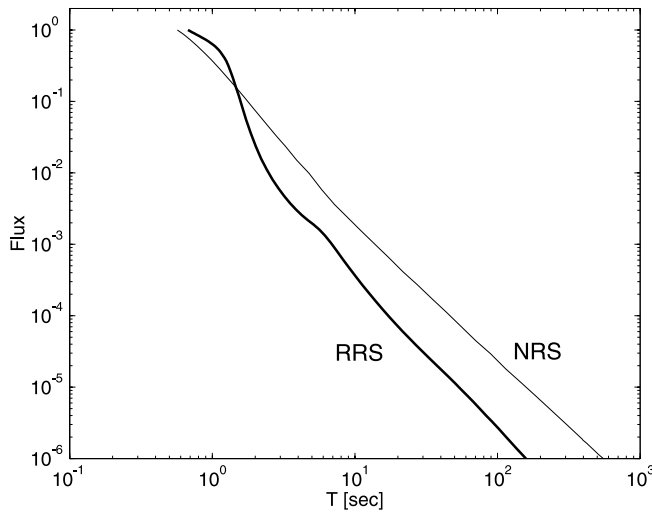
FIG. 6.—Light curves as emitted from the cooling ejecta, that was earlier heated by the reverse shock. The light curves are normalized at the shock crossing time. Their typical frequencies are assumed to be below the observed frequency. Thick line gives the evolution in the RRS case ($\xi = 10^{-3}$) while thin line is the NRS evolution ($\xi = 44$). It can be seen that the RRS light curve is steeper in the beginning. When the temperature in the ejecta becomes nonrelativistic, it decreases more slowly as in the NRS case. See the electronic edition of the Journal for a color version of this figure.
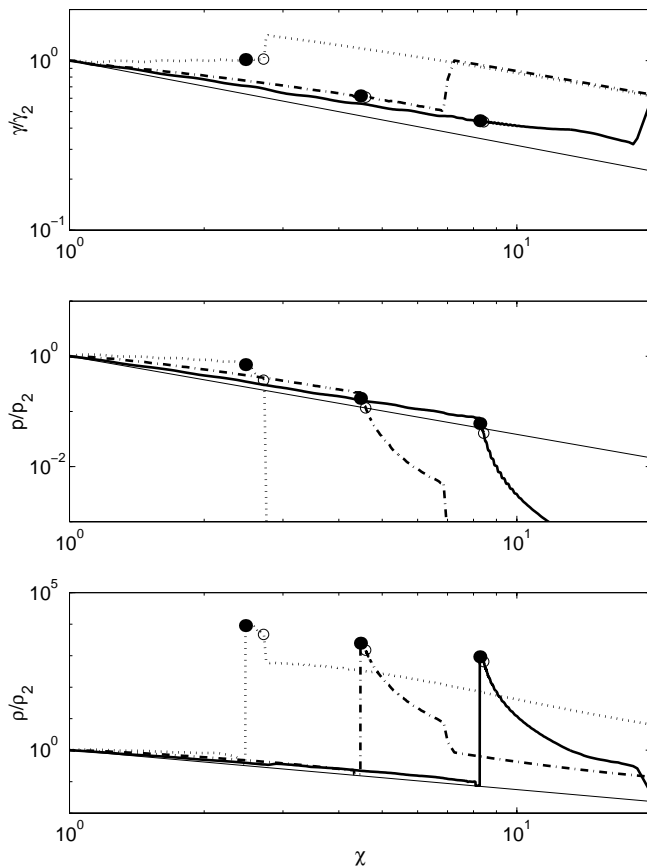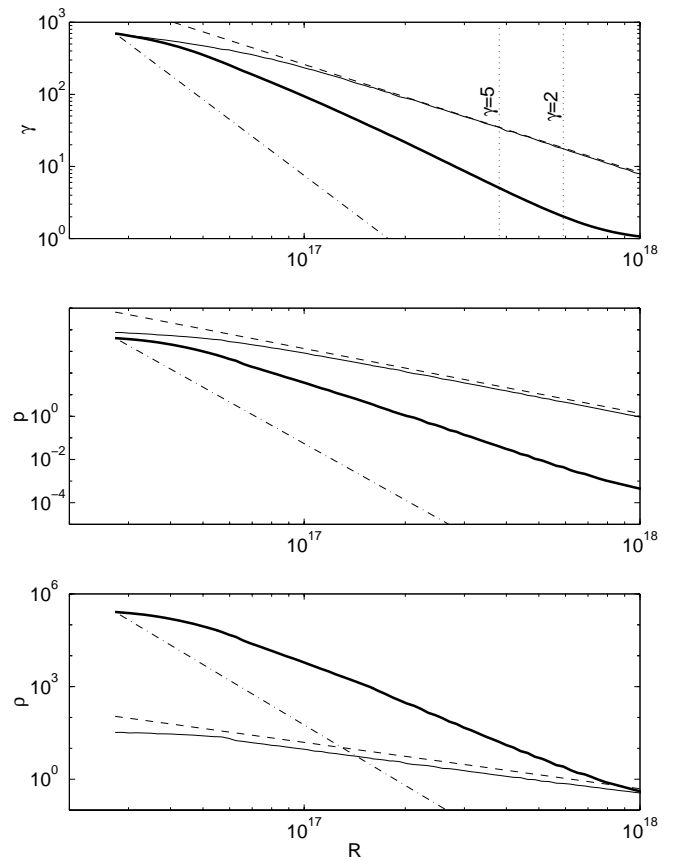


FIG. 8.—Evolution of Lorentz factor, pressure, and density: NRS case. The numerical values just behind the forward shock are the thin solid lines, the expected values by the Blandford-McKee solution are the thin dashed lines. The numerical evolution of the averaged values in the ejecta shell (*thick solid lines*) are compared with the Blandford-McKee scalings of a fluid element (*thin dash-dotted lines*). The vertical dotted lines show the radius where the Lorentz factor of the ejecta is 2 or 5. See the electronic edition of the Journal for a color version of this figure.



FIG. 7.—NRS case: Lorentz factor, pressure, and density as functions of $\chi$ at $R_{\Delta,\mathrm{num}}$ (*dotted lines*), at $2R_{\Delta,\mathrm{num}}$ (*dot-dashed lines*) and at $3R_{\Delta,\mathrm{num}}$ (*solid lines*). The Blandford-McKee solution is the thin solid lines. See the electronic edition of the Journal for a color version of this figure.

simulation is still valid to study the energy transfer stage due to relativistic beaming.

When the reverse shock crosses the ejecta around $R_{\Delta,\mathrm{num}} \sim 8.4 \times 10^{16}$ cm $\sim 0.9R_{\Delta}$, the Lorentz factor of the shocked regions is about 120. The reverse-shocked region is already cold from the beginning $e/\rho \sim 0.6$, while the forward-shocked region is hot $e/\rho \sim 120$. The temperature ratio is $\sim 200$ close to the analytic estimate $\eta\xi^{3/4} \sim 300$.

At $\sim 2R_{\Delta,\mathrm{num}}$ the forward-shocked region is well described by the BM scaling (see Fig. 10), the reverse-shocked region deviates from it. The reverse shock does not heat the shell as well as in the RRS case. At $R_{\Delta,\mathrm{num}}$, the boundaries of the shell are at $\chi = 2.5$ and 3.4, the analytic formula gives that the values are 40 and 54 at $2R_{\Delta,\mathrm{num}}$, 203 and 275 at $3R_{\Delta,\mathrm{num}}$. The numerical correspondences are 5.2 and 6.8 at $2R_{\Delta,\mathrm{num}}$, 16 and 19 at $3R_{\Delta,\mathrm{num}}$, considerably smaller.

The hydrodynamic variables of the shocked shell evolve slower than the BM (see Fig. 11). The vertical dotted lines show the times when the Lorentz factor of the ejecta shell becomes $\gamma = 5$ and $\gamma = 2$. These happen at 0.55 and 6.2 days, respectively, for the observer. The effective scaling index of $\gamma$ is about 2.2, which is the same to that of the NRS case (see Fig. 12). The analytic estimates (eq. [2]) are a good approximation again as long as the bulk motion is relativistic.
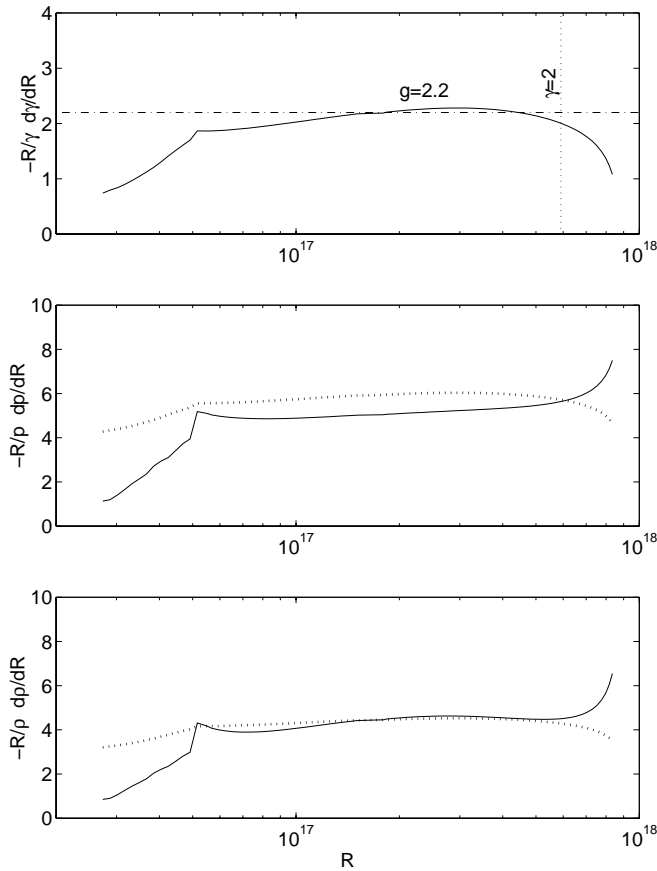
Fig. 9.—Effective scaling indexes vs. Radius of the shell: NRS case. The numerical results are the solid lines. The dotted lines in the middle and the bottom panel are analytic estimates assuming the numerical index $g$. See the electronic edition of the Journal for a color version of this figure.



Fig. 10.—GRB 990123: Lorentz factor, pressure, and density as functions of $\chi$ at $R_{\Delta,\text{num}}$ (*dotted lines*), at $2R_{\Delta,\text{num}}$ (*dot-dashed lines*) and at $3R_{\Delta,\text{num}}$ (*solid lines*). The Blandford-McKee solution is the thin solid lines. See the electronic edition of the Journal for a color version of this figure.

Using a normalization 1.7 Jy at the peak and the numerical evolutions of $\gamma$, $p$, and $\rho$, the optical light curve is plotted in Figure 13. The ROTSE observations are also plotted (*stars*), and the arrows give the upper limits. This normalization value of 1.7 Jy is double of the second ROTSE observation 0.81 Jy, it gives good fits to both of the optical flash and the radio flare. The normalization is actually done at the radio flare.

The numerical light curve reasonably fits the observation, the numerical light curve also qualitatively shows a steeper initial decline. We have simulated the evolutions of fireballs for different initial parameters to find that the numerical light curves are determined by two parameters: $R_0$ and $\xi$. The peak time of the optical flash is given by $\max[R_0/c, \xi^2 R_0/c]$ within a factor of a few. The initial deviation from $T^{-2}$ depends on $\xi$ (see Fig. 6).

Though the behavior of the fireball shell depends weakly on the explosion energy and the ambient density, the actual values of these quantities for GRB 990123 is rather uncertain. If we assume a much higher explosion energy or a much lower ambient density than we have assumed, the light curve fits the observations better, because the initial deviation from $T^{-2}$ is smaller in a case of $\xi \gg 1$. However, this is inconsistent with the burst duration. In the GRB 990123 event, the flash happened during the burst. Since the burst duration is given by $\sim R_0/c$, it is not allowed to choose such a small $R_0$ to fit the peak time of the flash, $\sim \xi^2 R_0/c$, to the observation in a large $\xi$ case.
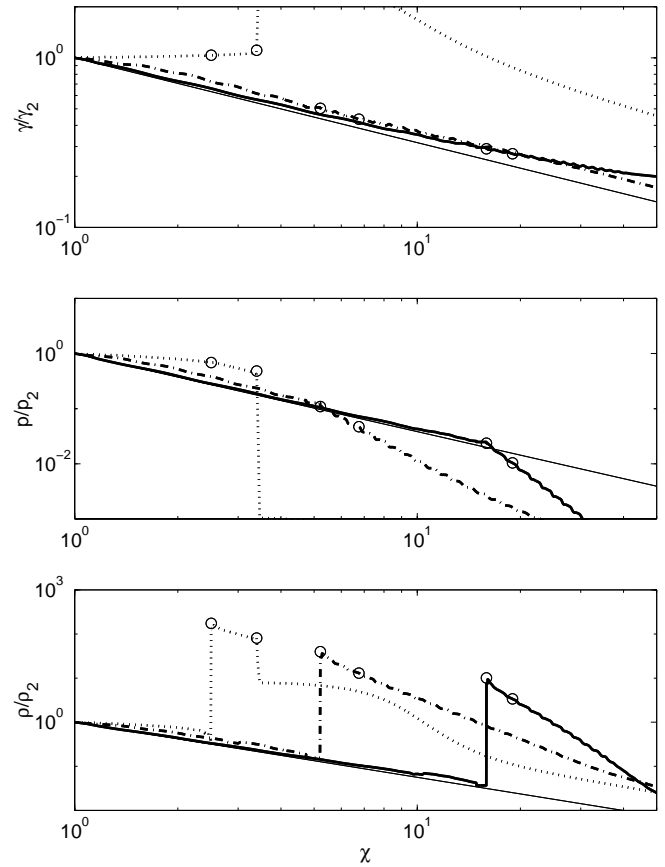
The deviation in Figure 13 can have several causes. The second observation of ROTSE has been assumed to be just at the peak, but the observation is sparse and the exposure duration is 5 s. It is also possible that the real peak is in between the second (47 s) and the third (72 s) ROTSE data. This will allow the higher peak value. A more fundamental problem is that in the internal shocks model, the source is not a single explosion. At the end of the internal shock phase (GRB phase) we are left with a rather ordered flow in which faster ejecta are the outermost ones and slower follow behind them. At the afterglow phase the outermost ones are decelerated by the ISM, the slower ones collide into them. This effect makes the decay of the light curve slower (Rees & Mészáros 1998; Panaitescu, Mészáros, & Rees 1998; Sari & Mészáros 2000). Even in a case that most shells have merged to form a single one in the GRB phase, a large inhomogeneity of the density profile causes a similar effect.

Emission from the reverse shock can also explain the radio flare, the radio detection 1 day after the burst (Sari & Piran 1999c; Kulkarni et al. 1999). The shocked ejecta initially radiates in the optical band. As the ejecta expands, the temperature of the ejecta becomes lower. The emission frequency and the flux drop quickly; eventually the emission comes to the radio band and further lower.

We use the same normalization with the optical flash estimate, the flux of 1.7 Jy at the typical frequency $\nu_m = 5 \times 10^{14}$ Hz at 52 s. The peak frequency $\nu_m \propto \gamma p^{5/2} \rho^{-2}$ reaches 8.5 GHz after 12 hr, the peak flux $F_{\nu_m} \propto \gamma p^{1/2}$ is 1.5
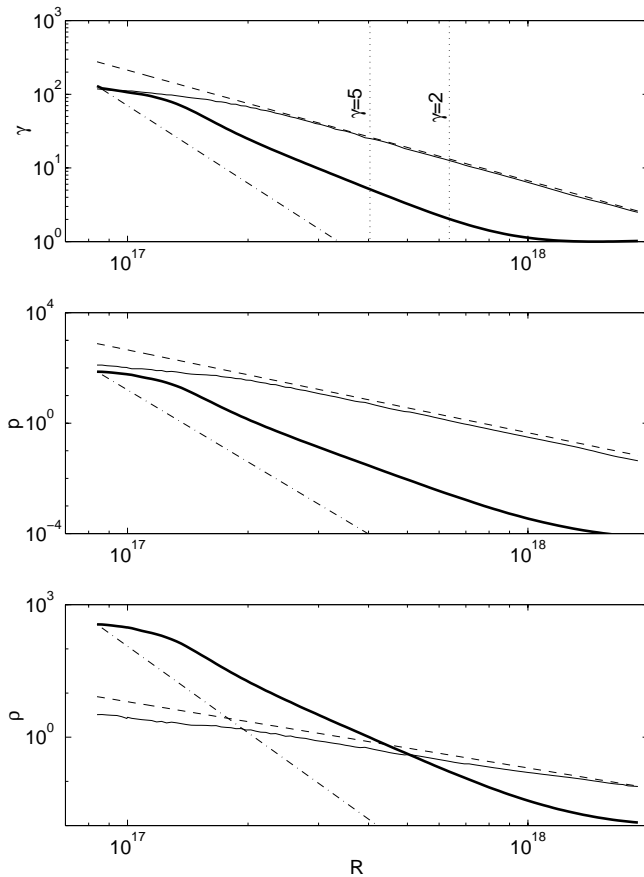
FIG. 11.—Evolution of Lorentz factor, pressure, and density: GRB 990123. Numerical values just behind the forward shock (*thin solid line*), expected values by the Blandford-McKee solution (*thin dashed line*), averaged values in the ejecta (*thick solid lines*) and the Blandford-McKee scalings of a fluid element (*thin dash-dotted line*). The vertical dotted lines show the radius where the Lorentz factor of the ejecta is 2 or 5. See the electronic edition of the Journal for a color version of this figure.

mJy at that time. After that the flux at the radio band drops as $\propto \gamma^{(\hat{p}+1)/2} p^{(5\hat{p}-3)/4} \rho^{-(\hat{p}-1)}$. The flux at 8.5 GHz is plotted in Figure 14.

Self-absorption can reduce the radio flux. Using equation (4) with $\epsilon_e = 0.6$ (Granot, Piran, & Sari 1999), the upper limit is numerically estimated (Fig. 14, *dot-dashed line*). When accounting for this, the resulting emission is the minimum between the solid line and the dot-dashed line. The estimates fit very well to the radio observation. Since the emission is normalized with the observation, only the evolution scalings of the hydrodynamic variables are important to estimate it. On the other hand, the self-absorption estimate (eq. [4]) depends on the absolute values. It is relatively sensitive to the Lorentz factor and the temperature of the ejecta.

## 5. DISCUSSION

We have studied numerically the evolution of fireballs. Specifically, we focused on the evolution of the reverse-shocked ejecta which is causing the optical flash and the radio flare of GRB 990123. We have seen that the Blandford-McKee solution is not applicable to the shocked ejecta in a NRS case in which the reverse shock is Newtonian or mildly relativistic and the temperature of the shocked ejecta is not relativistic. However, in a RRS case in
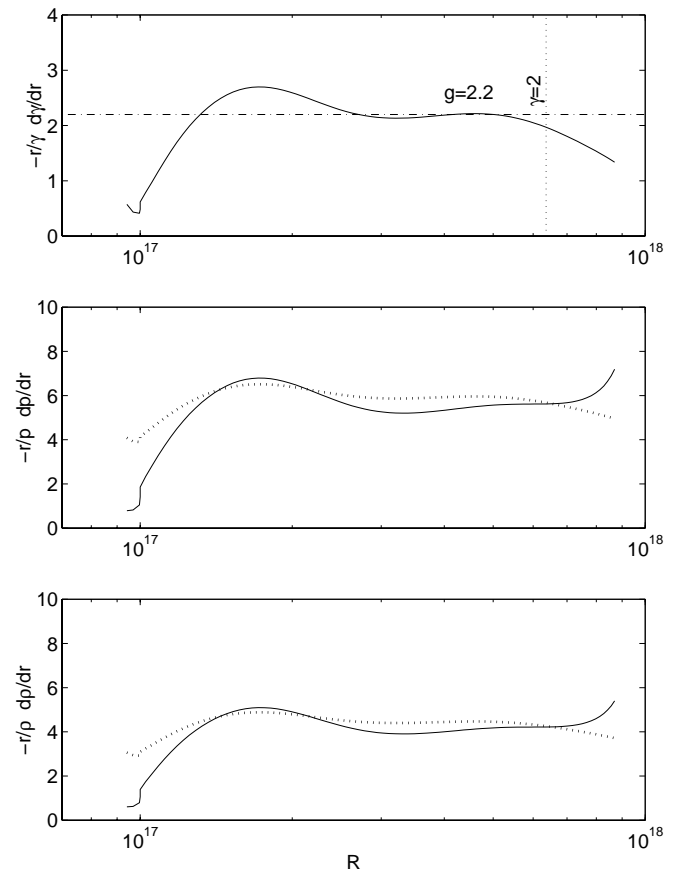


FIG. 12.—Effective scaling indexes vs. Radius of the shell: GRB 990123. The numerical results are the solid lines. The dotted lines in the middle and the bottom panel are analytic estimates assuming the numerical index $g$. See the electronic edition of the Journal for a color version of this figure.

which the reverse shock is relativistic, the profile of the reverse-shocked ejecta as well as the forward-shocked ISM approached to the solution after the reverse shock had crossed the ejecta. The self-similar solution is rigorous only after the details of the initial conditions becomes no longer
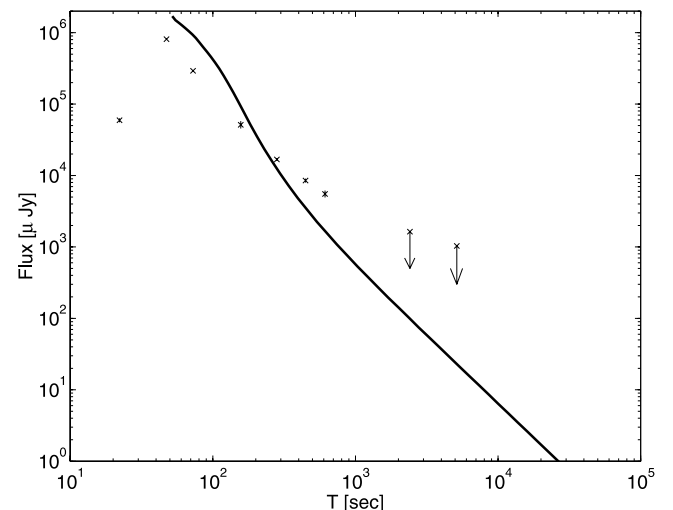


FIG. 13.—Optical light curve: GRB 990123. The solid line depicts the numerical light curve. The stars are the ROTSE observations and the arrows show the upper limits. See the electronic edition of the Journal for a color version of this figure.
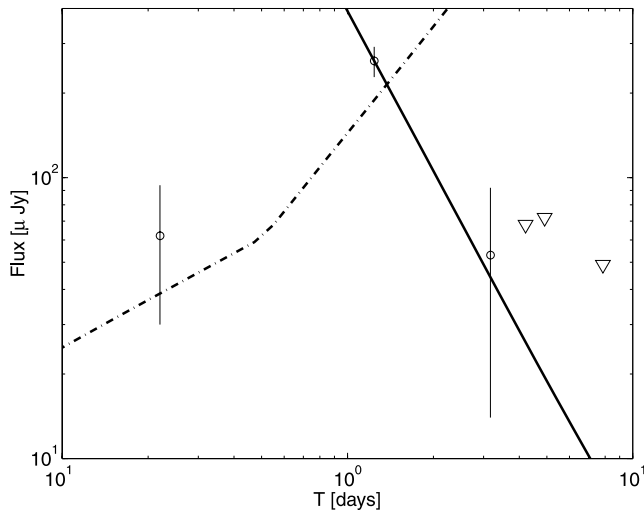
Fig. 14.—Radio light curve: GRB 990123. Numerical light curve (*solid line*), self-absorption upper limit (*dot-dashed line*). Observations are also plotted, triangles are upper limits. See the electronic edition of the Journal for a color version of this figure.

important. We find that initially a steeper decline may be expected, qualitatively compatible with the observations of GRB 990123.

The hydrodynamics of the cold shocked ejecta is very different from that of the hot shocked ejecta which is well described by the Blandford-McKee solution. The numerical scaling relations for a cold one were well approximated by the spreading assumption and the adiabatic expansion law, while the Blandford-McKee solution satisfies the relativistic version of it. We have estimated the radiation from the fireball ejecta in both cases: cold and hot shells. Surprisingly, we find that both evolutions give rather similar light curves even though the hydrodynamics is very different.

After the reverse shock crossed the ejecta shell, the electrons cool due to the adiabatic expansion, the emission frequency and the flux drop quickly. The radio flare, the single radio detection 1 day after the burst is the late time correspondence to the early optical flash. Using the numerical results we have shown that the reverse shock can explain the radio flare observation a day after the burst, in agreement with the previous analytical estimates.

The late time afterglow is less sensitive to the property of the original ejecta, which is determined by only one parameters, the ratio between the explosion energy and the density of the ambient medium. The new observation window, the optical flash is very useful to probe the original ejecta and ultimately the inner engine producing it. Future optical flash and radio flare observations will enable us to know about the original ejecta more. Numerical simulations similar to the one presented here will be useful for the detailed study.

REFERENCES

Akerlof, C. W., et al. 1999, GCN Circ. 205 (http://gcn.gsfc.nasa.gov/gcn/gcn3/205.gcn3)
Blandford, R. D., & McKee, C. F. 1976, Phys. Fluids, 19, 1130 (BM)
Galama, T. J., et al. 1999, Nature, 398, 394
Granot, J., Piran, T., & Sari, R. 1999, ApJ, 527, 236
Kippen, R. M., et al. 1999, GCN Circ. 224 (http://gcn.gsfc.nasa.gov/gcn/gcn3/224.gcn3)
Kobayashi, S., Piran, T., & Sari, R. 1997, ApJ, 490, 92
———. 1999, ApJ, 513, 669
Kulkarni, S. R., et al. 1999, Nature, 398, 389

Mészaros, P., & Rees, M. J. 1997, ApJ, 476, 231
———. 1999, MNRAS, 306, L39
Panaitescu, A., Mészaros, P., & Rees, M. J. 1998, ApJ, 503, 314
Rees, M. J., & Mészaros, P. 1998, ApJ, 496, L1
Sari, R., & Mészaros, P. 2000, preprint (astro-ph/0003406)
Sari, R., & Piran, T. 1995, ApJ, 455, L143
———. 1999a, A&AS, 138, 537
———. 1999b, ApJ, 520, 641
———. 1999c, ApJ, 517, L109